

1 Revision 1

2

3 To: American Mineralogist

7/6/18

4

5

6

7

8

9

10

11

12

13

14 Solution mechanisms of COHN fluids in melts to upper mantle
15 temperature, pressure, and redox conditions

16

17

18

19

20

21

22

23

24

25

Bjorn Mysen
Geophysical Laboratory
Carnegie Instn. Washington
Washington DC 20015
USA

26 **Abstract**

27
28 In order to advance our knowledge of speciation among volatiles during melting and
29 crystallization in the Earth's interior, the nature of carbon-, nitrogen-, and hydrogen-bearing
30 species was determined in COHN fluids and dissolved in coexisting aluminosilicate melts.
31 Micro-Raman characterization of fluids and melts were conducted in-situ while samples were at
32 temperature up to 825°C and pressure up to ~1400 MPa under redox conditions controlled with
33 the Ti-TiO₂-H₂O hydrogen fugacity buffer. The fluid species are H₂O, H₂, NH₃, and CH₄. In
34 contrast, under oxidizing conditions the species are H₂O, N₂ and CO₂.

35 The equilibria among silicate structures (Q-species) and reduced carbon and nitrogen
36 species are, $2\text{NH}_3 + 4\text{Q}^n \rightleftharpoons 2\text{Q}^{n-1}(\text{NH}_2) + 2\text{Q}^{n-1}(\text{OH})$, and $2\text{CH}_4 + 4\text{Q}^n \rightleftharpoons 2\text{Q}^{n-1}(\text{CH}_3) + 2\text{Q}^{n-1}(\text{OH})$. The Qⁿ- and Qⁿ⁻¹ denote silicate species with, respectively, n and n-1 bridging oxygens.
37 The formulation in parentheses, (NH₂), (CH₃), and (OH), is meant to indicate that those
38 functional groups replace one or more oxygen in the silicate tetrahedra. There is no evidence for
39 O-NH₂ or O-CH₃ bonding. Therefore, solution of reduced C- and N-species species in the COHN
40 system results in depolymerization of silicate melts. The ΔH-values derived from the X_{NH₂}/X_{NH₃}
41 and X_{CH₃}/X_{CH₄} evolution with temperature, respectively, were 8.1±2.3 kJ/mol and between -
42 4.9±1.0 and -6.2±2.2 kJ/mol.

44 The fluid/melt partition coefficients, K^{fluid/melt}, of the reduced species, H₂O, H₂, NH₃, and
45 CH₄, remain above unity at all temperatures. For example, for carbon it is in the 6-15 range with
46 a ΔH = -13.4±2.4 KJ/mol. These values compare with a 0.8-3 range with ΔH = -19±2.4 kJ/mol
47 in N-free silicate-COH systems. The K^{fluid/melt}-values for reduced nitrogen and molecular
48 hydrogen are in the 6-10 and 6-12 range with ΔH-values of -5.9±0.9 kJ/mol and =8±6 kJ/mol,
49 respectively.

50 A change in redox conditions during melting and crystallization in the Earth sufficient to
51 alter oxidized to reduced carbon- and nitrogen-bearing species will affect all melt properties that
52 depend on melt polymerization. This implies that changing redox conditions during melting of a
53 COHN-bearing mantle can have profound effect on physical and chemical properties of melts
54 and on melting and melt aggregation processes.

55

56 **Introduction**

57 An understanding of the behavior of COHN volatiles in magmatic systems at high temperature and
58 pressure is central to characterization of processes that describe formation and evolution of the
59 solid Earth, recycling of volatiles, and interaction between the solid Earth and its oceans and
60 atmosphere (Zhang and Zindler, 1993; Miyazaki et al., 2004; Adler and Williams, 2005; Sata et
61 al., 2010). These processes and the underlying materials properties needed for modeling are
62 governed by temperature, pressure, redox conditions, and bulk chemistry. Redox conditions can
63 affect the carbon and nitrogen distribution and recycling because they can exist in different
64 oxidation states within the range of redox conditions in the Earth's interior (Miyazaki et al.,
65 2004; Mysen et al., 2008; Mysen and Fogel, 2010; Kadik et al., 2011, 2015). Under highly
66 reducing conditions, molecular H₂ also becomes an important species.

67 Under reducing conditions, distribution of nitrogen in the Earth is governed in part by its
68 solubility in crystalline phases where NH₄⁺ functional groups can substitute for K⁺ in the crystal
69 structure of mica and amphibole, for example (Duit et al., 1986; Watenpuhl et al., 2009) and in
70 part by solubility of (N...H) complexes in melts and fluids. The nitrogen partitioning behavior
71 between and solubility in minerals, melts, and fluids at high pressure and temperature also is
72 important, and depends on the oxidation state of nitrogen (Libourel et al., 2003; Miyazaki et al.,
73 2004; Bebout et al., 2013).

74 Redox-dependent speciation of C-bearing volatile components also affects properties of
75 magmatic systems. For example, melting of oxidized CO₂- and CO₃²⁻-bearing upper mantle
76 yields silica-undersaturated melts such as alkali olivine basalt and nephelinite and perhaps even
77 carbonatite (Hirose, 1997; Dalton and Wood, 1993). However, with the hydrogen fugacity
78 conditions greater than that of the MW (Fe₃O₄/FeO/H₂O) buffer, the stable C-species in COH-

79 bearing melts at high pressure and temperatures are CH₄ and CH₃⁻ groups (Mysen et al., 2011).
80 Such redox conditions are not unusual in the mantle of the present Earth (Carmichael and
81 Ghiorso, 1990). The potential importance of reduced C-bearing species in the modern Earth
82 notwithstanding, only a handful of experimental studies aimed to characterize the melting
83 behavior of methane-bearing silicate systems at high pressure has been reported. What is known
84 suggests that methane lowers activity coefficients of silica, which would drive composition of
85 partial melt towards silica enrichment, for example (Eggler and Baker, 1982; Taylor and Green,
86 1989).

87 Molecular H₂ is a major component under hydrogen fugacity conditions equivalent to the IW
88 (Fe/FeO)+H₂O buffer and above. It may, therefore, have been an important fluid component at
89 the redox conditions of the early Earth. Significant concentrations of molecular H₂ is less
90 important in the modern Earth (O'Neill, 1991) where the necessary high f_{H₂}-conditions are rare.

91 An understanding of the role of COHN volatiles during the formation and evolution of the
92 Earth requires experimentally-determined speciation (structure) of volatiles in and their
93 partitioning between fluids and melts under conditions of the Earth's interior. Recently developed
94 methods that rely on externally-heated diamond anvil cell technology coupled with vibrational
95 spectroscopy have made it possible to obtain such data (Bassett et al., 1994; Zotov and Keppler,
96 2002; Mibe et al., 2008). In the present report, fluid and melt structure and fluid/melt partitioning
97 of volatile components silicate- COHN systems have been carried out with such techniques.

98

99 **Experimental Methods**

100 Experiments were carried out with the samples contained in a 500 μm diameter central hole of a
101 125 μm thick Ir gasket placed between the diamonds culets in the hydrothermal diamond anvil

102 cell (Bassett et al., 1994). Starting materials were glass chips of the alkali aluminosilicate
103 composition $(\text{Na}_2\text{Si}_4\text{O}_9)_{90}(\text{Na}_2(\text{NaAl})_4\text{O}_9)_{10}$ that were mixed with $\text{Ag}_2\text{C}_2\text{O}_4$ and AgN_3 and loaded
104 into the hydrothermal diamond anvil cell together with double-distilled, dionized H_2O and small
105 pieces of Ti metal. Carbon dioxide and N_2 were formed from decomposition of the silver oxalate
106 ($\text{Ag}_2\text{C}_2\text{O}_4$) and silver azide (AgN_3), which takes place near 200°C . Condensed materials (silicate
107 + $\text{Ag}_2\text{C}_2\text{O}_4$ + AgN_3 +Ti metal) represented about 50% of the starting composition together with
108 about 50% liquid H_2O . However, these proportions could not be determined with precision
109 because of the small sample volume ($<0.0x \mu\text{m}^3$).

110 During an experiment, the Ti metal reacted with H_2O to control the hydrogen fugacity via the
111 reaction:

112



114

115 This CO_2 and N_2 were transformed to CH_4 and NH_3 by reaction with H_2 from the f_{H_2} buffer
116 reaction [eqn. (1)] (Mysen and Fogel, 2010; Foustoukos and Mysen, 2013);

117



119



121

122 Molybdenum wire wrapped around each of two SiC diamond seats was used to form heaters.
123 Temperature was monitored with two K-type thermocouples touching the diamonds about 1-1.5
124 mm from the sample. Temperature variations, determined with the melting point of NaCl
125 (800.5°C at ambient pressure), is $\sim\pm 2^{\circ}\text{C}$. Pressure, generated by the fluid at essentially constant
126 volume in the sample chamber, changed with temperature. It was monitored with the one-phonon
127 Raman shift of synthetic ^{13}C diamond added as small chips to the sample volume (Schiferl et al.,
128 1997). Pressure was, therefore, a temperature-dependent variable (Table 1). The ^{13}C diamond
129 was used in order to avoid interference from the Raman spectra from the natural diamonds in the
130 diamond anvil cell itself. Pressure/temperature-dependence of the one-phonon Raman shift was
131 calibrated against the equation-of-state of pure H_2O by Mysen and Yamashita (2010). The
132 pressure uncertainty, which includes both spectrometer precision and fitting errors in the
133 calibration, is about ± 110 MPa. The spectrometer precision alone translates to a pressure
134 precision of ± 40 MPa. Pressure does not decrease monotonously with decreasing temperature
135 because there was some deformation of the Ir gasket hole, which, therefore, resulted in sample
136 volume changes and, therefore, pressure variations.

137 Fluid and melt structure was evaluated from Raman spectra recorded with a JASCO model
138 NRS-3100 confocal microRaman spectrometer. With this system, a 2.5 cm working-distance
139 50X by 0.42 N.A. objective lens was used. The samples were excited with the 490 nm line of a
140 solid-state laser operating at ~ 30 mW at the sample. With this spectrometer set-up, the optical
141 resolution was 2-3 μm across by about 30 μm depth. The spectrometer is equipped with a single
142 monochromator, holographic notch filter, and holographic gratings. Gratings with 1200 and 2400
143 grooves/mm were employed. The 2400 grooves/mm gratings were used together with Ne

144 emission lines for frequency reference to collect high-precision carbon-13 diamond spectra with
145 $\pm 0.1 \text{ cm}^{-1}$ uncertainty. Measurements of the melt and fluid samples were carried out with 1200
146 grooves/mm and 2-3 cm^{-1} frequency uncertainty. The data were recorded with an Andor Model
147 DV401-F1 Peltier-cooled CCD.

148 Several temperature/pressure series of measurements were carried out. For each series, the
149 sample was first brought to the highest planned temperature and pressure and kept at this
150 condition (825°C and ~1400 MPa in the present case) for ~60 minutes, which is sufficient to
151 attain equilibrium for which only several minutes are needed (Horita, 2014). Spectroscopic
152 measurements of the sample (fluid, melt, and/or supercritical fluid) and the ^{13}C diamond were
153 carried out at the highest planned temperature and pressure before the temperature was reduced
154 at 1°C/s cooling rate to the next temperature. Pressure decreased accordingly (Table 1). The
155 measurement protocol was then repeated. Each experimental data point was 75°C apart with the
156 last measurements at 525°C and 634 MPa. Ambient conditions Raman measurements of the ^{13}C
157 diamond were carried before and after a series of high-temperature and -pressure experiments.

158

159 **Results**

160 For each temperature and pressure, spectra were recorded from about 400 cm^{-1} to 4200 cm^{-1} in
161 order to include frequencies of most (Si,Al)-O vibrations and vibrations in species involving
162 COHN components (Fig. 1). The band assignments in this and subsequent figures are based
163 predominantly on Nakamoto (1997). The peaks marked 1st and 2nd order diamond are from the
164 diamonds in the diamond anvil cell itself. There are no ^{13}C diamond signals the Raman spectra of
165 fluids and melts because carbon-13 diamond spectra were recorded separately.

166 The individual Raman band intensities differ significantly (Fig. 1). Therefore, in order to
167 make the topology of the peaks and their variations with temperature and pressure more visible,
168 the spectra have been divided into 4 segments, marked A, B, C, and D as indicated in Fig. 1, and
169 expanded in separate figures.

170 The frequency region, A, is from about 400 cm^{-1} to the strong one-phonon band from
171 diamond located near 1300 cm^{-1} (Figs. 1 and 2). It comprises signals assigned to (Si,Al)-O
172 vibrations as well as some of the bending modes of COHN species. In the spectra of fluids (Fig.
173 2A), this frequency regime is dominated by three bands, near 600 , 800 , and 1030 cm^{-1} . At the
174 highest temperatures, there is also a weak shoulder near 770 cm^{-1} . The integrated intensities of
175 the three main bands decrease with decreasing temperature and pressure while their frequencies
176 remain essentially constant (average frequencies: 591 ± 2 , 813 ± 3 , and $1030.4\pm 0.5\text{ cm}^{-1}$,
177 respectively). The 591 cm^{-1} band is assigned to Si-CH₃ stretching, and the other two to bending
178 vibrations in NH₂ functional groups (Fig. 2A). Additional support for Si-CH₃ bonds can be found
179 in recent ¹³C MAS NMR data from quenched aluminosilicate melts equilibrated with
180 CH₄+H₂O+H₂ fluid at 1.5 GPa and 1400°C under reducing conditions (Mysen et al., 2011). The
181 770 cm^{-1} shoulder is assigned to Si-O⁻ stretching in isolated SiO₄ entities (also denoted Q⁰).

182 The spectra of melt are dominated by a broad band (FWHH ~80 cm^{-1}) at 885 cm^{-1} and
183 weaker and broad bands near 485 , 570 , and 1035 cm^{-1} (Fig. 2B). The 885 cm^{-1} band is assigned
184 to Ti-O vibrations from Ti⁴⁺ dissolved formed by oxidation of Ti metal [eqn. (1)].

185 The 485 cm^{-1} band is assigned to Si-O-Si rocking in Q⁴ species and the 570 cm^{-1} band to Si-
186 O-Si bending most likely in Q³ species (Furukawa et al., 1981; McMillan et al., 1992). The
187 existence of polymerized silicate species in the melts also is indicated by the broad band above

188 1000 cm^{-1} (FWHH near 100 cm^{-1}), which is assigned to Si-O stretching in polymerized species in
189 melts, most likely dominated by Q^3 type (McMillan et al., 1992). A more detailed review of the
190 band assignments assigned to (Si,Al)-O vibrations can be found in chapters 7 and 12 of Mysen
191 and Richet (2005).

192 The region between the 1st and 2nd order Raman peaks from the diamond cell diamonds
193 (near 1330 and 2600 cm^{-1} , respectively) is denoted segment B (Figs. 1 and 3). The spectra of
194 fluid are dominated by a sharp peak (FWHH: 10-15 cm^{-1}) near 1440 cm^{-1} (Fig. 3A). Its intensity
195 decreases with decreasing temperature. In melt spectra, this peak is only seen in those from the
196 highest temperature and pressure (825°C/1400 MPa; see Fig. 3B). It is assigned NHN bending in
197 NH_3 molecules (Nakamoto, 1997). The fluid spectra also show a sharp peak near 1640 cm^{-1} ,
198 which could be assigned to HNH bending vibrations in NH_3 molecules (Colthup et al., 1990;
199 Nakamoto, 1997). The fluid spectra at 825° and 750°C also show a sharp peak slightly above
200 1800 cm^{-1} . Although an assignment is quite uncertain, it cannot be ruled out that this is from C-O
201 vibrations in CO groups perhaps from carboxylic acid (Colthup et al., 1990). The only other peak
202 common to spectra of both fluids and melts in the B-region occurs near 1550 cm^{-1} (Figs. 3A, B),
203 which is assigned HOH bending in H_2O molecules (Nakamoto, 1997; Efimov and Pogareva,
204 2006).

205 In the spectra of fluid, the C-region extends from the high-frequency side of the 2nd-order
206 peak of diamond cell diamonds near 2600 cm^{-1} to the beginning of the low-frequency tail of the
207 strong peak centered between 3500 and 3600 cm^{-1} (Figs. 1 and 4). There are two peaks, near
208 2900 cm^{-1} and 3320 cm^{-1} , in the spectra of melts and fluids (Figs. 4A and B). There is also a
209 weak and broad band centered near 3240 cm^{-1} in the spectra of fluids (Fig. 4A). The 2900 cm^{-1}
210 band is asymmetric toward lower frequency. This asymmetry can be accommodated by fitting

211 two Gaussian lines, near 2895 cm^{-1} and 2910 cm^{-1} (Fig. 6). These two peaks are assigned to C-H
212 stretching in, respectively, CH_3 groups and CH_4 molecules (Nakamoto, 1997), similar to that
213 reported from Raman spectra of Al-free melts by Mysen and Yamashita (2010) and in the Raman
214 and ^{13}C MAS NMR spectra of aluminosilicate glasses equilibrated as melts under reducing
215 conditions and temperature-quenched to glass (Mysen et al., 2011).

216 The two peaks near 3300 cm^{-1} are expanded with Gaussian lines fitted to spectra in the
217 example in Fig. 6. The strongest band, at 3325 cm^{-1} , is assigned to N-H stretching in NH_3
218 molecules, whereas the weaker and broader band, near 3230 cm^{-1} , is assigned to N-H stretching
219 in NH_2 groups (Yeo and Ford, 1994; Nakamoto, 1997; Mysen et al., 2008). There is no evidence
220 for NH_4^+ because the N-H stretch frequencies from this functional group is in the $3000\text{-}3200\text{ cm}^{-1}$
221 frequency range (Socrates, 2001; Mysen et al., 2008), in which range there are no Raman bands
222 in the present spectra.

223 Frequency region D extends from the intense band centered between 3500 and 3600 cm^{-1} and
224 a group of bands of lesser intensities near $4100\text{-}4150\text{ cm}^{-1}$ (Fig. 7). This latter group is assigned
225 the Q-branch of H_2 reflecting vibrational to rotational transitions (Veirs and Rosenblatt, 1987;
226 Schmidt et al., 1998). The $3500\text{-}3600\text{ cm}^{-1}$ peak is assigned to OH stretching in OH groups
227 bonded to cations such as Si^{4+} , Al^{3+} , and Na^+ as well as OH groups in molecular H_2O (see also
228 Nowak and Behrens, 1994; Kawamoto et al., 2004).

229

230

231 **Discussion**

232 *Solution mechanisms of reduced COHN species*

233 The solution mechanisms of reduced carbon and nitrogen in silicate-COH melts and silicate-
234 NOH melts, respectively, involve various combinations of C..H and N..H complexes (Kadik et
235 al., 2004; Mysen et al., 2008, 2011; Ni and Keppler, 2013; Armstrong et al., 2015). For melts and
236 fluids in silicate-COHN systems, little is known except for some recent data obtained in-situ
237 under oxidizing conditions (Mysen, 2018). In the latter case, the sole nitrogen species was N₂ so
238 that nitrogen simply acted as a diluent of the other gas species. Carbon existed as CO₂ and as
239 CO₃²⁻ groups.

240 The solution behavior of reduced carbon-bearing species has been developed with the aid of
241 the simple expressions based on the interpretation of ¹³C MAS NMR spectra of quenched silicate
242 melt-COH (e. g., Mysen et al., 2011);

243



245

246 and for reduced nitrogen in silicate melt-NOH systems (Mysen et al., 2008);

247



249

250 In equations (4) and (5), O^{2-} represents oxygen in the silicate structural network. It is linked to
251 silicate speciation via the expression,

252



254

255 where Q^n and Q^{n-1} denote silicate species with, respectively n and $n-1$ bridging oxygen, and,
256 therefore, $4-n$ and $3-n$ nonbridging oxygen.

257 By combining equations (4) and (6), we have;

258



260

261 which describes the relations between dissolved CH_3 groups and the silicate structure. From the
262 carbon-13 MAS NMR and Raman spectroscopic data of quenched melts, Mysen et al., (2011)
263 concluded that CH_3 groups thus formed substitute for oxygen in the silicate tetrahedra because
264 there was evidence of CH_3 and CH_4 groups, but no evidence for Si-O-C bonding environments.
265 Therefore, $2Q^{n-1}(CH_3)$ and $2Q^{n-1}(OH)$ denote depolymerized silicate tetrahedra with at least one
266 of the oxygens replaced by CH_3 and OH groups, respectively. This interpretation is also
267 consistent with the assignment of the Raman band near 600 cm^{-1} (Fig. 2).

268 For reduced nitrogen-bearing components, by combining equations (5) and (6), we have;

269



271

272 The Si-NH₂ interpretation relies on the assignment of the ~800 cm⁻¹ band in Fig. 2 to be an NH₂
273 bending mode (Nakamoto, 1997). In other words, the exchange of NH₂ groups for oxygen in
274 silicate tetrahedra cleaves oxygen bridges to form Si-NH₂ and Si-OH bonds, which results in
275 silicate depolymerization.

276 There is also the equilibrium between molecular H₂O and OH⁻ groups that describes a
277 principal solution mechanism of H₂O in melts (e.g., Stolper, 1982);

278



280

281 Equation (9) combined with equation (6), yields the equilibria involving silicate (Q-species)
282 H₂O, and OH groups;

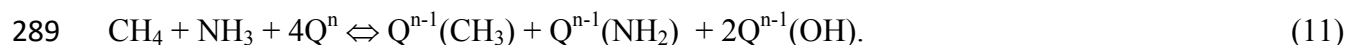
283



285

286 By combining equations (7) and (8), the solution equilibrium among COHN species in
287 silicate fluids (and probably melts) under reducing conditions becomes;

288



290

291 Equation (11) does not take into account interaction of H₂ with the silicate network. Such
292 interaction, through formation of Si-H and Si-OH bonds, is possible via a schematic formulation
293 such as (Van der Steen and Van den Boom, 1977);

294



296

297 Si-H stretch vibrations would result in Raman bands in the 2100-2200 cm⁻¹ region (Schmidt et
298 al., 1998) in addition to the OH fundamental stretch vibrations giving rise to the 3500-3600 cm⁻¹
299 envelope. The former frequency is within the frequency range of 2nd-order Raman scattering of
300 diamonds from the diamond cell, whereas the OH vibrations yield the same signal as OH
301 vibrations from the other H₂O in the system. Whether or not there are contributions from Si-H
302 and Si-OH from eqn. (12) cannot, therefore, be ascertained. Given this lack of information,
303 further speculation and adjustments to eqn. (11) does not seem justified.

304 The equilibrium among silicate melt and COHN volatiles under reducing conditions differs
305 significantly from that under oxidizing conditions where nitrogen simply dissolves as molecular
306 N₂ and acts as a diluent (Mysen, 2018). The H₂O equilibrium remains same, and molecular CO₂
307 is in equilibrium with carbonate groups, CO₃²⁻ (Morizet et al., 2015);

308



310

311 so that by combining equations (9, 10, 13), we have;

312



314

315 Here, nitrogen as N₂ is shown on both sides of the equation simply to indicate that it behaves as
316 an inert component. It follows that under oxidizing conditions even in the presence of H₂O, in
317 silicate-COHN systems CO₂ dissolves to form CO₃²⁻, which results in silicate polymerization.

318 The proportion of molecular and structurally bound species such as discussed above can be
319 determined from the Raman spectra with the assumption that for a specific vibration (e.g.,
320 stretching or bending etc.), the Raman cross sections are the same for vibrations in the molecule
321 and structurally bound functional groups (CH₄/CH₃ and NH₃/NH₂) and that the C-H and N-H
322 vibrations in these groups are localized thus not being significantly affected by the neighboring

323 electronic environments. Ratios of integrated Raman intensity ratios from a given type of
324 vibration in the two species then equals their abundance ratio. For $X_{\text{CH}_3}/X_{\text{CH}_4}$ [eqn (4)], for
325 example, this intensity ratio is that of the C-H stretch vibrations near 2900 cm^{-1} (2895 and 2910
326 cm^{-1});

327

$$328 \quad X_{\text{CH}_3}/X_{\text{CH}_4} = A_{2895}/A_{2910}. \quad (15)$$

329

330 In spectra of fluids, the $X_{\text{CH}_3}/X_{\text{CH}_4}$ ratio increases with increasing temperature (Fig. 8), from
331 which an enthalpy of $8.1 \pm 2.3 \text{ kJ/mol}$ can be extracted. In other words, in COHN fluids in
332 equilibrium with aluminosilicate melts, equation (4) shifts to the right with increasing
333 temperature. The spectra of melts are insufficiently resolved to extract such information.

334 The $X_{\text{NH}_2}/X_{\text{NH}_3}$ in fluid was calculated from a similar treatment of the Raman data (Fig. 9).
335 Two sets of $X_{\text{NH}_2}/X_{\text{NH}_3}$ data were extracted from the spectra of fluid from bands assigned to NH_2
336 and NH_3 bending motions in the low-frequency region and from those assigned to N-H stretching
337 in NH_3 and NH_2 near 3300 cm^{-1} (Fig. 2A). These slopes result in ΔH -values of -4.9 ± 1.9 and -
338 $6.2 \pm 2.2 \text{ kJ/mol}$. We note here that the temperature evolution of the $X_{\text{NH}_2}/X_{\text{NH}_3}$ abundance ratio is
339 opposite of $X_{\text{CH}_3}/X_{\text{CH}_4}$. In other words, whereas equation (4) shifts to the right with temperature
340 thus enhancing the abundance of molecular CH_4 , equation (5) shifts to the left so that molecular
341 NH_3 becomes increasingly abundant. Interestingly, under oxidizing conditions, the CO_2/CO_3
342 equilibrium [eqn. (13)] also shifts toward increasing abundance of molecular CO_2 with
343 increasing temperature (Nowak et al., 2003).

344

345 *Fluid/melt partitioning*

346 Water. The partition coefficient for H₂O between fluid and melt, when calculated from integrated
347 intensity of the 3600 cm⁻¹ band (O-H stretching) in coexisting fluids and melts, is a non-linear
348 function of 1/T and less than unity (Fig. 10). This behavior contrasts with the H₂O partitioning in
349 silicate-COHN under oxidizing conditions where $K^{\text{fluid/melt}}_{\text{H}_2\text{O}} > 1$ and is a linear function of 1/T
350 (Mysen, 2018). This difference likely is because under reducing conditions TiO₂ from the redox
351 reaction (1) dissolves in significant amounts in melts (but not in fluid), which results in the very
352 broad and asymmetric 3600 cm⁻¹ band (Figs. 1 and 10). The TiO₂ concentration in the melt likely
353 changes with temperature and pressure. This results in a non-linear temperature-dependent
354 $K^{\text{fluid/melt}}_{\text{H}_2\text{O}}$.

355

356 Methane. The partition coefficients for methane between coexisting fluid and melt are expressed
357 in terms as, $\Sigma C = \text{CH}_3 + \text{CH}_4$ (Fig. 11) because separate contributions from CH₄ and CH₃ cannot
358 be quantified from the spectra of melt. Methane partitions into fluid relative to melt. The
359 partition coefficients for the CH₃+CH₄ components are not necessarily the same as total carbon
360 because of the suggested CO groups in the highest-temperature fluids (Fig. 3). However, given
361 the lack of relevant Raman signals in spectra of melts as well as in the low-temperature fluid
362 spectra, contributions from such carbon was not considered. This also means that the $K_{\Sigma C}^{\text{fluid/melt}}$ -
363 values (Fig. 11) may be minimum values.

364 The partition coefficient decreases with increasing temperature (and pressure), which results
365 in $\Delta H = -13.4 \pm 2.3$ kJ/mol by assuming no pressure effect. This value compares with a ΔH -value
366 of -19 ± 2.9 for the fluid/melt partition coefficient with the same bulk silicate, but without
367 nitrogen in the system (Mysen, 2015). The offset between the two data sets likely reflects the
368 different pressure/temperature paths in the two experimental series as well as the absence of
369 nitrogen species in fluids and melts in the silicate-COH system by Mysen (2015).

370

371 Ammonia. Qualitatively, the fluid/melt partition coefficient for total reduced nitrogen ($\Sigma N =$
372 $NH_3 + NH_2$) decreases with increasing temperature. This behavior is similar to the temperature-
373 dependent $K_{\Sigma C}^{\text{fluid/melt}}$ (Figs. 11 and 12). The enthalpy value extracted from the temperature-
374 dependence with the assumption of no detectable pressure dependence is -5.9 ± 0.9 kJ/mol.

375

376 Hydrogen. The H_2 fluid/melt partition coefficient ranges between ~ 6 and ~ 10 in the temperature
377 and pressure range examined (Fig. 13). There is a slight decrease with increasing temperature
378 and pressure, but the data scatter is significant thus leading to an enthalpy value with large
379 uncertainty, -8 ± 6 kJ/mol.

380

381 **Implications**

382 Reduction of carbon and nitrogen in silicate-COHN melts at high temperature and pressure
383 occurs under conditions near and more reducing those defined by the MW+H₂O buffer (Mysen et

384 al., 2008, 2011). Under such conditions the dominant fluid species are H₂O, H₂, NH₃, and CH₄.
385 That behavior differs from oxidizing conditions where H₂O, N₂ and CO₂ are the principal
386 species. and where CO₂ may be in equilibrium with CO₃²⁻ and HCO₃⁻ groups, or both.

387 A change in redox conditions sufficient to alter oxidized to reduced carbon- and nitrogen-
388 bearing species during melting and crystallization in the Earth will affect all melt properties that
389 depend on melt polymerization [see solution mechanisms illustrated with equations (9) and (12)].
390 Examples of such melt properties are viscosity, diffusion, and density (Baker et al., 2005;
391 Behrens, 2010; Seifert et al., 2013). Crystal/melt element partitioning also is linked to melt
392 polymerization (Jaeger and Drake, 2000) and, therefore, the redox conditions during melting and
393 crystallization in the presence of COHN fluids. Melt polymerization is also linked to activity of
394 silicate, which means a change in redox conditions will lead to a change in melting and
395 crystallization phase relations (Moretti and Papale, 2004). This latter feature sometimes is termed
396 redox melting.

397

398 **Acknowledgments**

399 This research was conducted with support from NSF grant EAR-1212754.

400

401 **References**

- 402
- 403 Adler, J.F., and Williams, Q. (2005) A high-pressure X-ray diffraction study of iron
404 nitrides: Implications for Earth's core. *J. Geophys. Res.*, 110, DOI:
405 10.1029/2004JB003103.
- 406 Armstrong, L.S., Hirschmann, M.M., Stanley, B.D., Falksen, E.G., and Jacobsen, S.D.
407 (2015) Speciation and solubility of reduced C-O-H-N volatiles in mafic melt:
408 Implications for volcanism, atmospheric evolution, and deep volatile cycles in the
409 terrestrial planets. *Geochimica et Cosmochimica Acta*, 171, 283-302.
- 410 Baker, D.R., Freda, C., Brooker, R.A., and Scarlato, P. (2005) Volatile diffusion in
411 silicate melts and its effects on melt inclusions. *Annalen Geophysik*, 48, 699-717.
- 412 Bassett, W.A., Shen, A.H., Bucknum, M., and Chou, I.M. (1994) A new diamond cell for
413 hydrothermal studies to 2.5 GPa and from -190°C to 1200°C. *Reviews of Scientific*
414 *Instruments* 64, 2340-2345.
- 415 Bebout, G.E., Fogel, M.L., and Cartigny, P. (2013) Nitrogen: Highly Volatile yet
416 Surprisingly Compatible. *Elements*, 9, 333-338.
- 417 Behrens, H. (2010) Ar, CO₂ and H₂O diffusion in silica glasses at 2 kbar pressure.
418 *Chemical Geology*, 272(1-4), 40-48.
- 419 Carmichael, I.S.E., and Ghiorso, M.S. (1990) Controls on oxidation-reduction relations in
420 magmas. In J. Nicholls, and J.K. Russell, Eds. *Modern Methods of Igneous*
421 *Petrology: Understanding Magmatic processes*, p. 191-212. The Mineralogical
422 Society of America, Washington, DC.
- 423 Colthup, N.B., Daly, L.H., and Wiberley, S.E. (1990) *Introduction to Infrared and Raman*
424 *Spectroscopy*. 542 p. Academic Press, San Diego, CA.
- 425 Dalton, J.A., and Wood, B.J. (1993) The compositions of primary carbonate melts and
426 their evolution through wall rock reaction in the mantle. *Earth and Planetary*
427 *Science Letters* 119, 511-525.
- 428 Duit, W., Jansen, J.B.H., Van Breemen, A., and Bos, A. (1986) Ammonium micas in
429 metamorphic rocks as exemplified by Done de l'Agout (France). *American Journal*
430 *of Science.*, 286, 702-732.
- 431 Efimov, A.M., and Pogareva, V.G. (2006) IR absorption spectra of vitreous silica and
432 silicate glasses: The nature of bands in the 1300 to 5000 cm⁻¹ region. *Chemical*
433 *Geology*, 229, 198-217.
- 434 Eggler, D.H., and Baker, D.R. (1982) Reduced volatiles in the system C-H-O:
435 Implications to mantle melting, fluid formation and diamond genesis. *High-*
436 *Pressure Research in Geophysics*, 12, p. 237-250. D. Reidel / Kluwer Academic
437 Publishers, Boston / Dordrecht.
- 438 Foustoukos, D.I., and Mysen, B.O. (2013) Condensed-phase isotope effects on H/D
439 methane isotopologues dissolved in supercritical aqueous solution. *American*
440 *Mineralogist*, 98, 946-954.

- 441 Furukawa, T., Fox, K.E., and White, W.B. (1981) Raman spectroscopic investigation of
442 the structure of silicate glasses. III. Raman intensities and structural units in
443 sodium silicate glasses. *Journal of Chemical Physics*, 153, 3226-3237.
- 444 Hirose, K. (1997) Partial melt compositions of carbonated peridotite at 3 GPa and role of
445 CO₂ in alkali basalt generation. *Geophysical Research Letters*, 2837-2840.
- 446 Horita, J. (2014) Oxygen and carbon isotope fractionation in the system dolomite-water-
447 CO₂ to elevated temperatures. *Geochim. Cosmochim. Acta*, 129, 111-124.
- 448 Jaeger, W.L., and Drake, M.J. (2000) Metal-silicate partitioning of Co, Ga, and W;
449 dependence on silicate melt composition. *Geochimica et Cosmochimica Acta*,
450 64(22), 3887-3895.
- 451 Kadik, A., Pineau, F., Litvin, Y., Jendrzewski, N., Martinez, I., and Javoy, M. (2004)
452 Formation of carbon and hydrogen species in magmas at low oxygen fugacity.
453 *Journal of Petrology*, 45, 1297-1310.
- 454 Kadik, A.A., Kurovskaya, N.A., Ignat'ev, Y.A., Kononkova, N.N., Koltashev, V.V., and
455 Plotnichenko, V.G. (2011) Influence of Oxygen Fugacity on the Solubility of
456 Nitrogen, Carbon, and Hydrogen in FeO-Na₂O-SiO₂-Al₂O₃ Melts in Equilibrium
457 with Metallic Iron at 1.5 GPa and 1400 degrees C. *Geochemistry International*, 49,
458 429-438.
- 459 Kadik, A.A., Koltashev, V.V., Kryukova, E.B., Plotnichenko, V.G., Tsekhonya, T.I., and
460 Kononkova, N.N. (2015) Solubility of nitrogen, carbon, and hydrogen in FeO-
461 Na₂O-Al₂O₃-SiO₂ melt and liquid iron alloy: Influence of oxygen fugacity.
462 *Geochemistry International*, 53, 849-868.
- 463 Kawamoto, T., Ochiai, S., and Kagi, H. (2004) Changes in the structure of water deduced
464 from the pressure dependence of the Raman OH frequency. *Journal of Chemical*
465 *Physics*, 120, 5867-5870.
- 466 Libourel, G., Marty, B., and Humbert, F. (2003) Nitrogen solubility in basaltic melt. Part
467 I. Effect of oxygen fugacity. *Geochimica et Cosmochimica Acta*, 67, 4123-4136.
- 468 McMillan, P.F., Wolf, G.H., and Poe, B.T. (1992) Vibrational spectroscopy of silicate
469 liquids and glasses. *Chemical Geology*, 96, 351-366.
- 470 Mibe, K., and Bassett, W.A. (2008) In situ Raman spectroscopic investigation of the
471 structure of subduction-zone fluids. *Journal of Geophysical Research*, 113. DOI:
472 10.1029/2007JB005179.
- 473 Miyazaki, A., Hiyagon, H., Sugiura, N., Hirose, K., and Takahashi, E. (2004) Solubilities
474 of nitrogen and noble gases in silicate melts under various oxygen fugacities:
475 Implications for the origin and degassing history of nitrogen and noble gases in the
476 earth. 10.1029/2009GC002783, 68, 387-401.
- 477 Moretti, R., and Papale, P. (2004) On the oxidation state and volatile behavior in
478 multicomponent gas-melt equilibria. *Chemical Geology*, 213, 265-280.
- 479 Morizet, Y., Vuilleumier, R., and Paris, M. (2015) A NMR and molecular dynamics
480 study of CO₂-bearing basaltic melts and glasses. *Chemical Geology*, 418, 89-103.

- 481 Mysen, B. (2015) Carbon speciation in silicate-C-O-H melt and fluid as a function of
482 redox conditions: An experimental study, in situ to 1.7 GPa and 900 degrees C.
483 American Mineralogist, 100, 872-882.
- 484 Mysen, B. O. (2018) Mass Transfer in the Earth's Interior: Fluid-melt interaction in
485 aluminosilicate-C-O-H-N systems at high pressure and temperature under
486 oxidizing conditions. Progress in Earth and Planetary Science 5. DOI:
487 10.1186/s40645-017-0161-6
- 488 Mysen, B.O., and Fogel, M.L. (2010) Nitrogen and Hydrogen Isotope Compositions and
489 Solubility in Silicate Melts in Equilibrium with Reduced (N+H)-bearing Fluids at
490 High Pressure and Temperature: Effects of Melt Structure. American Mineralogist,
491 95, 987-999.
- 492 Mysen, B.O., Kumamoto, K., Cody, G.D., and Fogel, M.L. (2011) Solubility and solution
493 mechanisms of C-O-H volatiles in silicate melt with variable redox conditions and
494 melt composition at upper mantle temperatures and pressures. Geochimica et
495 Cosmochimica Acta. 75, 6183-6199.
- 496 Mysen, B.O., and Richet, P. (2005) Silicate Glasses and Melts - Properties and Structure.
497 548 p. Elsevier, New York.
- 498 Mysen, B.O., and Yamashita, S. (2010) Speciation of reduced C-O-H volatiles in
499 coexisting fluids and silicate melts determined in-situ to ~1.4 GPa and 800°C.
500 Geochimica Cosmochimica Acta, 74, 4577-4588.
- 501 Mysen, B.O., Yamashita, S., and Chertkova, N. (2008) Solubility and Solution
502 Mechanisms of NOH Volatiles in Silicate Melts at high Pressure and Temperature
503 - Amine Groups and Hydrogen Fugacity. American Mineralogist, 93, 1760-1770.
- 504 Nakamoto, K. (1997) Infrared and Raman Spectra of Inorganic and Coordination
505 Compounds. Part B. Applications in Coordination, Organometallic, and Bioorganic
506 Chemistry. 384 p. John Wiley & Sons, Inc., New York.
- 507 Ni, H.W., and Keppler, H. (2013) Carbon in Silicate Melts. Reviews in Mineralogy and
508 Geochemistry, 75, 251-287.
- 509 Nowak, M., and Behrens, H. (1995) The speciation of water in haplogranitic glasses and
510 melts determined by in-situ near-infrared spectroscopy. Geochimica et
511 Cosmochimica Acta, 59, 3445-3450.
- 512 Nowak, M., Porbatzki, D., Spickenbom, K., and Diedrich, O. (2003) Carbon dioxide
513 speciation in silicate melts: a restart. Earth and Planetary Science Letters, 207, 131-
514 139.
- 515 O'Neill, H.S.C. (1991) The origin of the Moon and the early history of the Earth - a
516 chemical model. Part 2: The Earth. Geochimica et Cosmochimica Acta, 55,
517 1159-1172.
- 518 Sata, N., Hirose, K., Shen, G., Nakajima, Y., Ohishi, Y., and Hirao, N. (2010)
519 Compression of FeSi, Fe₃C, Fe_{0.95}O, and FeS under the core pressures and

- 520 implication for light element in the Earth's core. *Journal of Geophysical Research*
521 115. DOI: 10.1029/2009JB006975
- 522 Schiferl, D., Nicol, M., Zaug, J.M., Sharma, S.K., Cooney, T.F., Wang, S.-Y., and
523 Fleischer, J.F. (1997) The Diamond $^{13}\text{C}/^{12}\text{C}$ Isotope Raman Pressure Sensor
524 System for High Temperature/Pressure Diamond-Anvil Cells with Reactive
525 Samples. *Journal of Applied physics*, 82, 3256-3265.
- 526 Schmidt, B.C., Holtz, F.M., and Beny, J.M. (1998) Incorporation of H_2 in vitreous silica,
527 qualitative and quantitative determination from Raman and infrared spectroscopy.
528 *Journal of Non-Crystalline Solids*, 240, 91-103.
- 529 Seifert, R., Malfait, W.J., Lerch, P., and Sanchez-Valle, C. (2013) Partial molar volume
530 and compressibility of dissolved CO_2 in glasses with magmatic compositions.
531 *Chemical Geology* 358, 119-130.
- 532 Stolper, E.M. (1982) The speciation of water in silicate melts. *Geochimica et*
533 *Cosmochimica Acta*, 46(12), 2609-2620.
- 534 Taylor, W.R., and Green, D.H. (1989) The role of reduced C-O-H fluids in mantle partial
535 melting. In J. Ross, Ed. *Kimberlites and Related Rocks - Their Composition,*
536 *Occurrence, Origin, and Emplacement*, 1, p. 592-602. Blackwell Scientific
537 Publishers, Carlton Australia.
- 538 Van der Steen, G.H.A.M., and Van den Boom, H. (1977) Raman spectroscopic study of
539 hydrogen-containing vitreous silica. *Journal of Non-Crystalline Solids*, 23, 279-
540 286.
- 541 Veirs, K.D., and Rosenblatt, G.D. (1987) Raman line positions in molecular hydrogen:
542 H_2 , HD , D_2 , DT , and T_2 . *Journal of Molecular Spectroscopy*, 121, 401-
543 419.
- 544 Watenpuhl, A., B., W., and Heinrich, W. (2009) High-pressure ammonium-bearing
545 silicates: Implications for nitrogen and hydrogen storage in the Earth's mantle.
546 *American Mineralogist*, 94, 283-292.
- 547 Yeo, G.A., and Ford, T.A. (1994) Ab initio molecular orbital calculations of the
548 energetic, structural, vibrational and electronic properties of some hydrogen
549 bonded complexes of water, ammonia and hydroxylamine. *Spectrochimica Acta*,
550 50A, 5-18.
- 551 Zhang, Y., and Zindler, A. (1993) Distribution and evolution of carbon and nitrogen in
552 the Earth. *Earth and Planetary Science Letters*, 117, 331-345.
- 553 Zotov, N., and Keppler, H. (2002) Silica speciation in aqueous fluids at high pressures
554 and high temperatures. *Chemical Geology*, 184, 71-82.
- 555

556 Table 1. Temperature/pressure conditions of experiments

557

558 Temperature, °C Pressure, MPa

559 25 0.1

560 525 634

561 600 594

562 675 554

563 750 1011

564 825 1414

565

566

567 **Figure Captions**

568 Figure 1 - Example of Raman spectra of coexisting melt and fluid at 525°C/634 MPa in the entire
569 spectral range studied. Intensity is normalized to cts/s. Band assignments are discussed in the
570 text. The frequency ranges marked A, B, C, and D show ranges that are expanded in subsequent
571 figures (and discussed in the text) to show better the spectral evolution.

572 Figure 2 - Raman spectra of coexisting fluid (A) and melt (B) in the frequency regime A (see
573 Fig. 1) as a function of temperature as seen on individual spectra and pressure as shown in Table
574 1. Band assignments are discussed in the text.

575 Figure 3 - Raman spectra of coexisting fluid (A) and melt (B) in the frequency regime B (see
576 Fig. 1) as a function of temperature as seen on individual spectra and pressure as shown in Table
577 1. Band assignments are discussed in the text.

578 Figure 4 - Raman spectra of coexisting fluid (A) and melt (B) in the frequency regime C (see
579 Fig. 1) as a function of temperature as seen on individual spectra and pressure as shown in Table
580 1. Band assignments are discussed in the text.

581 Figure 5 - Example of curve-fitted Raman spectrum of fluid in frequency regime C near 2900
582 cm^{-1} recorded at 825°C/1414 MPa.

583 Figure 6 - Example of curve-fitted Raman spectrum of fluid in frequency regime C near 3300
584 cm^{-1} recorded at 600°C/594 MPa.

585 Figure 7 - Raman spectra of coexisting fluid (A) and melt (B) in the frequency regime D (see
586 Fig. 1) as a function of temperature as seen on individual spectra and pressure as shown in Table
587 1. Band assignments are discussed in the text.

588 Fig. 8 - Evolution of abundance ratio, CH_3/CH_4 , in fluid as a function of temperature from fits to
589 the 2900 cm^{-1} region (see Table 1 for corresponding pressures). The straight line fit is described
590 with the expression, $\log(\text{CH}_3/\text{CH}_4) = -977 \pm 276/T(\text{K}) + 0.5 \pm 0.3$, $r^2 = 0.81$.

591 Fig. 9 - Evolution of abundance ratio, NH_2/NH_3 , in fluid as a function of temperature from fits
592 NHN stretching region between 3300 and 3200 cm^{-1} and NHN bending region between 600 and
593 1000 cm^{-1} (see Table 1 for corresponding pressures). The straight line fits are described with the
594 expressions: For NHN stretching $\log(\text{NH}_2/\text{NH}_3) = 595 \pm 230/T(\text{K}) - 1.1 \pm 1.2$, $r^2 = 0.69$, NHN
595 bending $\log(\text{NH}_2/\text{NH}_3) = 744 \pm 265/T(\text{K}) - 1.2 \pm 0.3$, $r^2 = 0.72$.

596 Fig. 10 - Fluid/melt partition coefficient for H_2O as a function of temperature (closed circles)
597 compared with results under oxidizing conditions

598 Fig. 11 - Fluid/melt partition coefficient for total carbon, ΣC , under reducing conditions
599 ($K^{\text{fluid/melt}} = 1617 \pm 281/T - 0.6 \pm 0.3$, $r^2 = 0.92$), under reducing conditions in silicate-COH ($K^{\text{fluid/melt}}$
600 $= 2283 \pm 347/T - 2.6 \pm 0.4$, $r^2 = 0.94$) (open circles; Mysen, 2015), and under oxidizing conditions in
601 silicate-COH ($K^{\text{fluid/melt}} = -3628 \pm 1630/T + 3.3 \pm 1.6$, $r^2 = 0.71$) (open diamonds; Mysen, 2015).

602 Fig. 12 - Fluid/melt partition coefficient for total nitrogen, ΣN , under reducing conditions
603 ($K^{\text{fluid/melt}} = 709 \pm 111 + 0.2 \pm 0.1$, $r^2 = 0.93$).

604 Fig. 13 - Fluid/melt partition coefficient for H_2 under reducing conditions ($K^{\text{fluid/melt}} = 1007 \pm 815 -$
605 0.1 ± 0.8 , $r^2 = 0.34$).

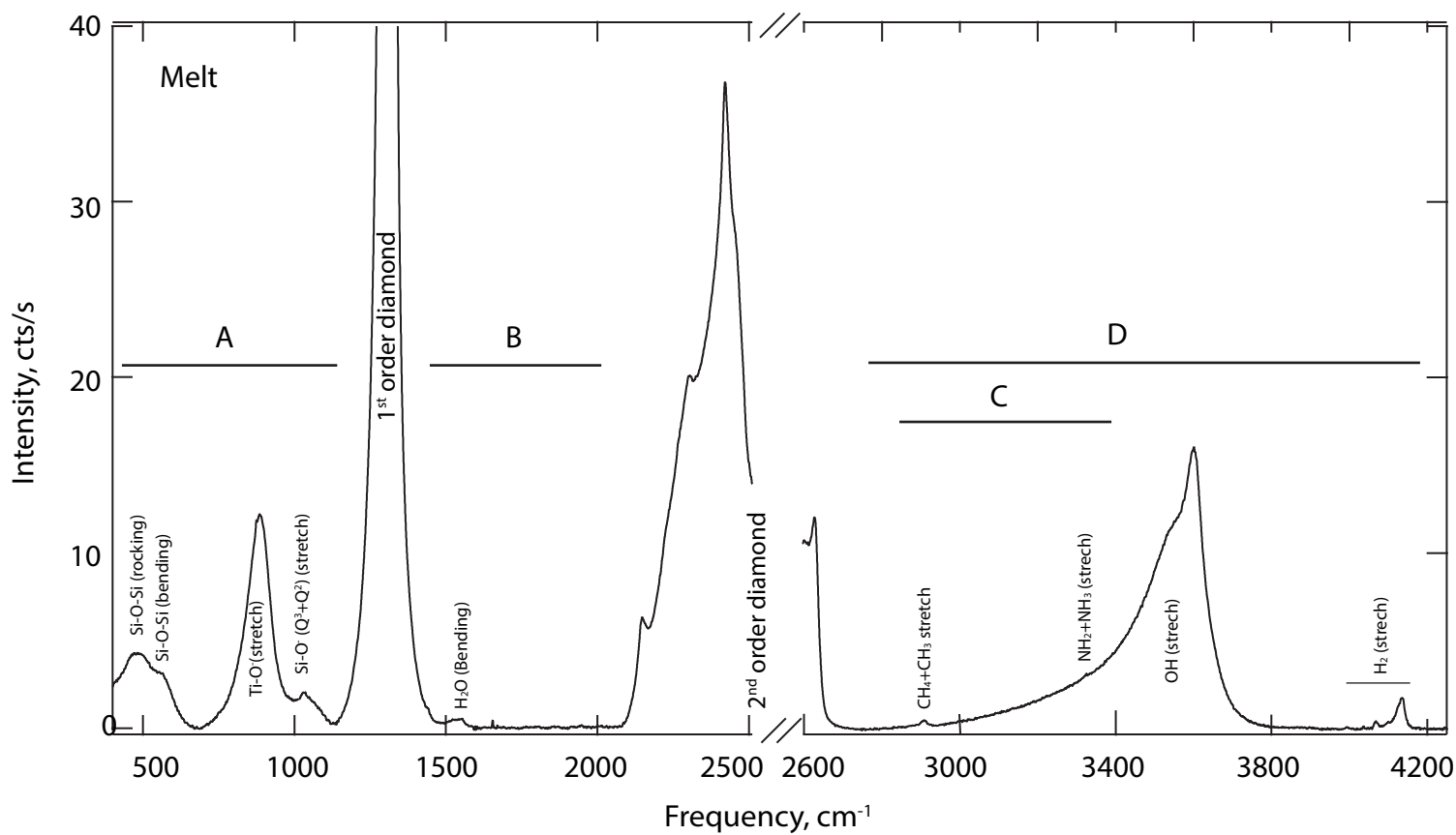
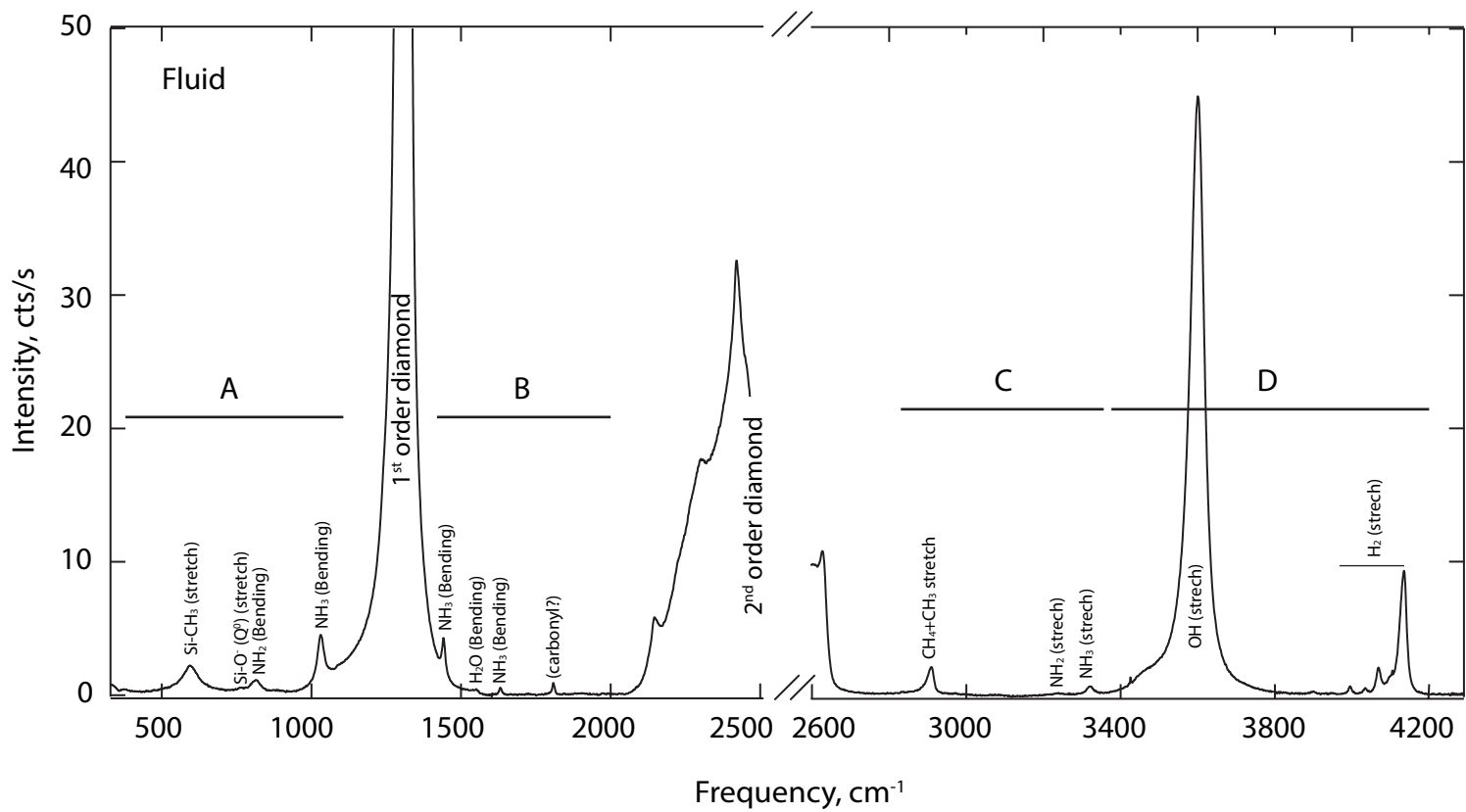


Figure 1

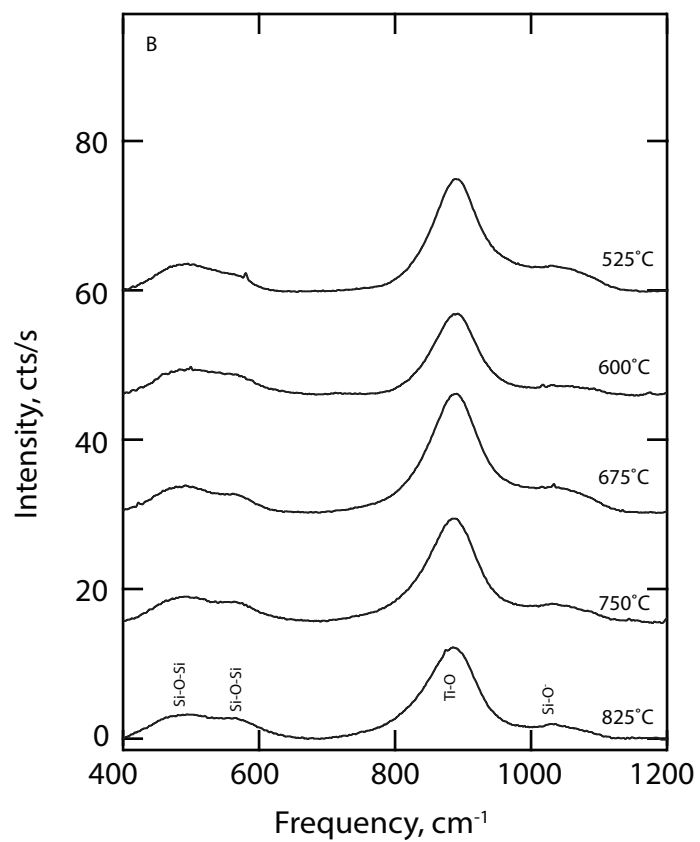
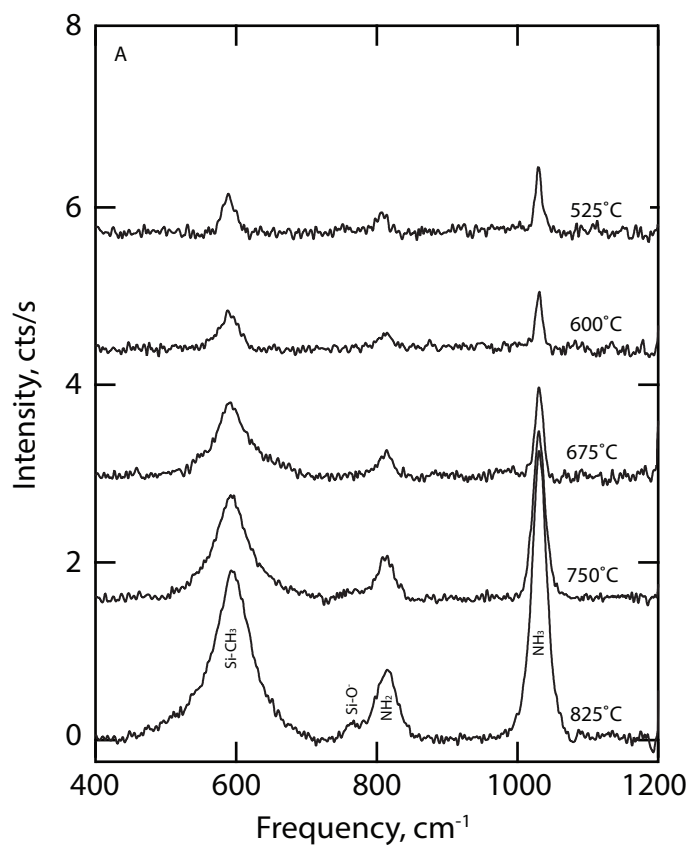


Figure 2

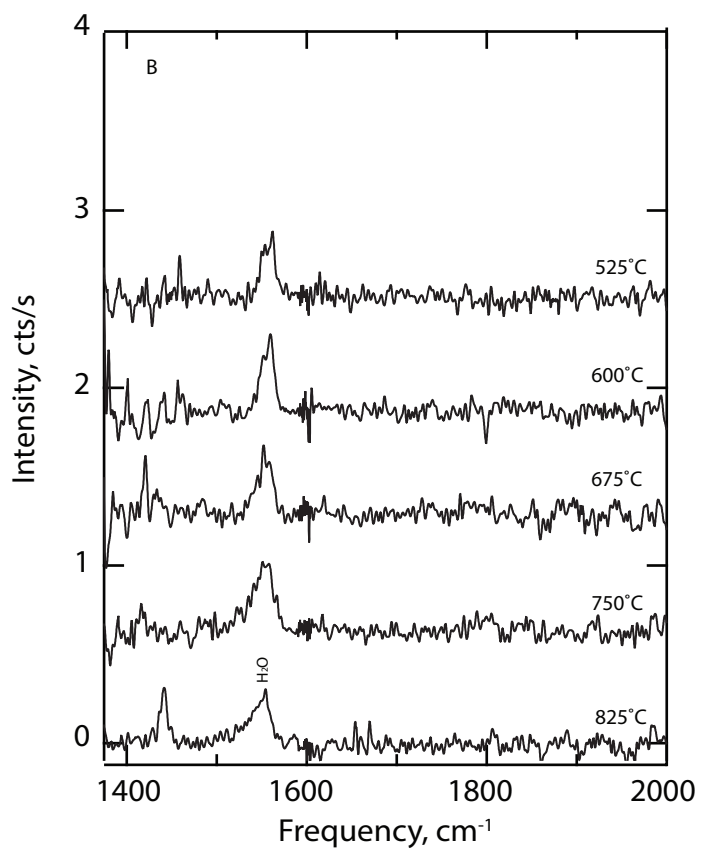
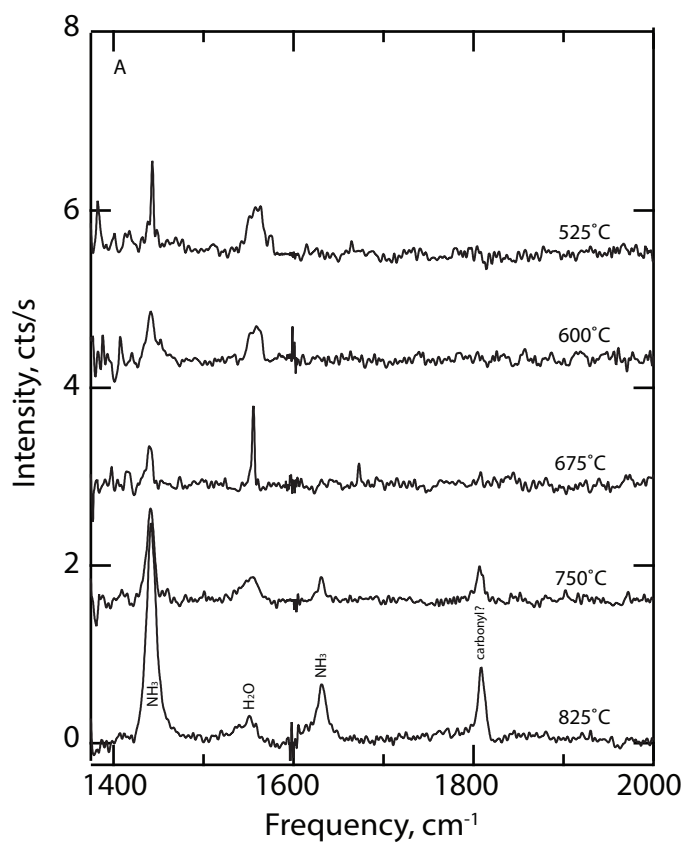


Figure 3

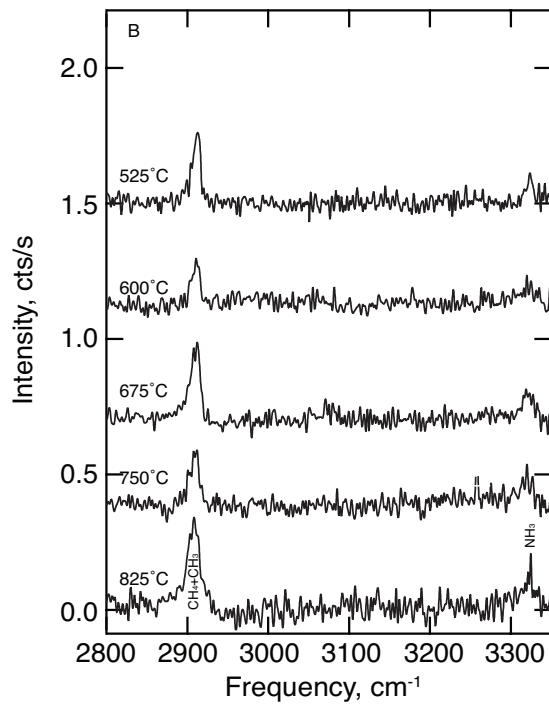
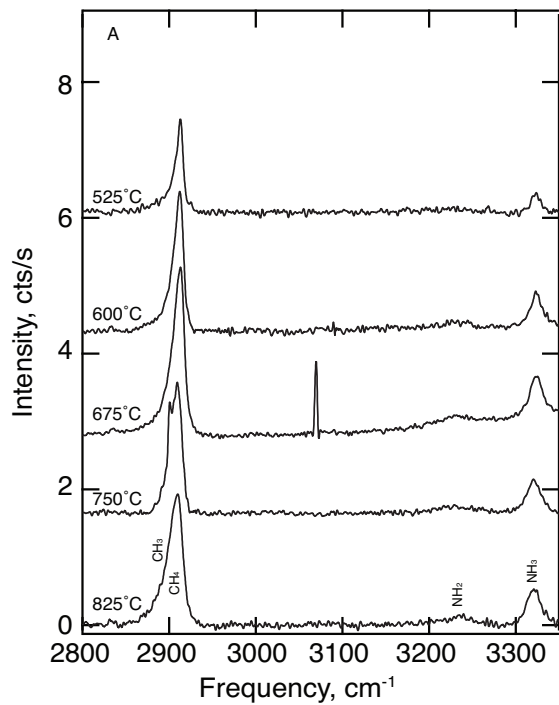


Figure 4

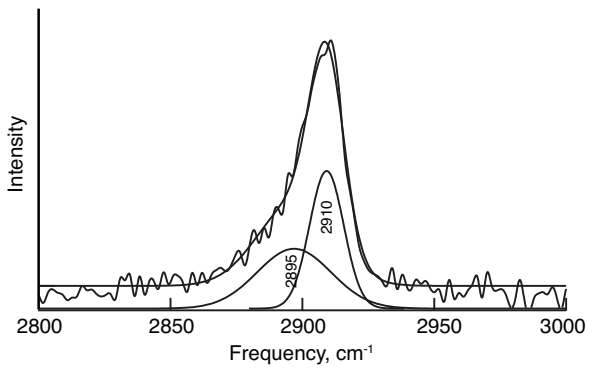


Figure 5

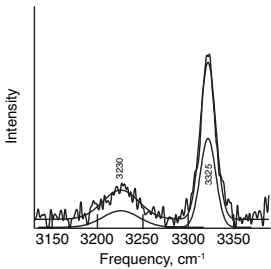


Figure 6

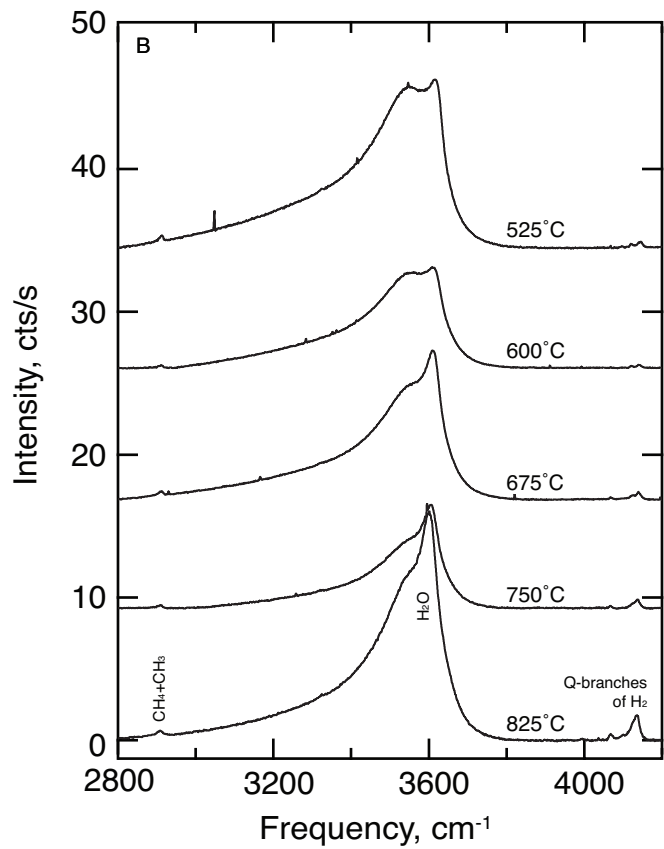
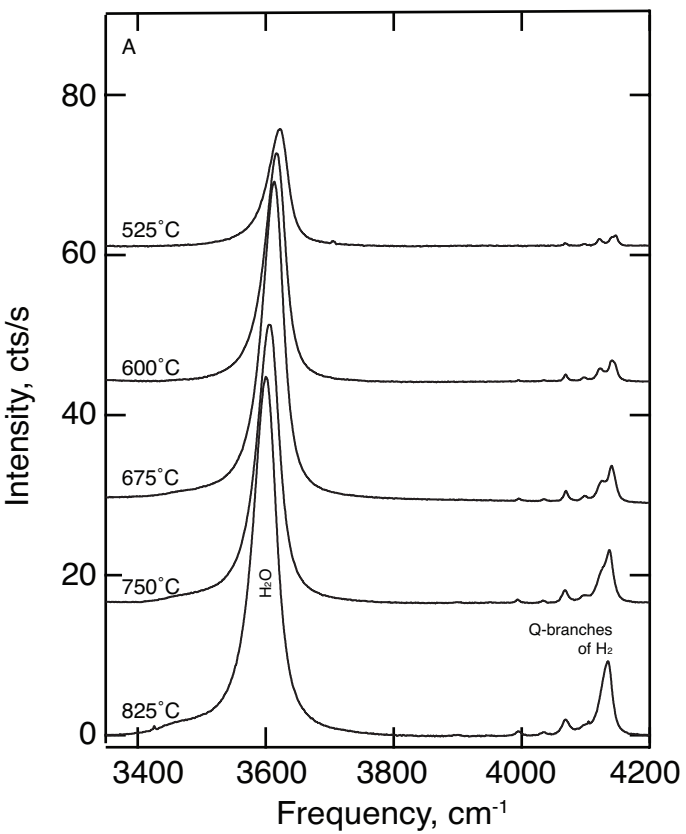


Figure 7

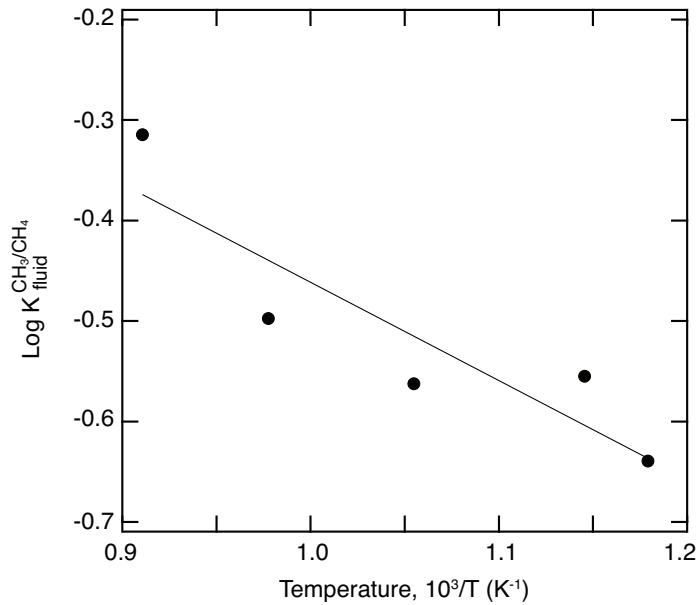


Figure 8

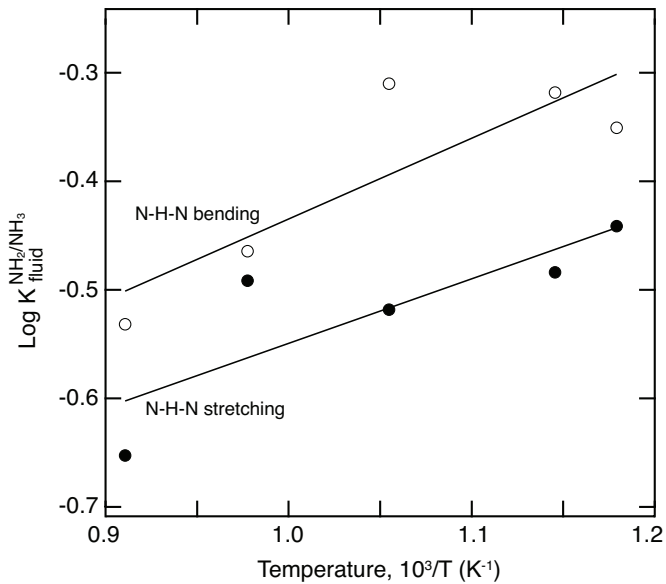


Figure 9

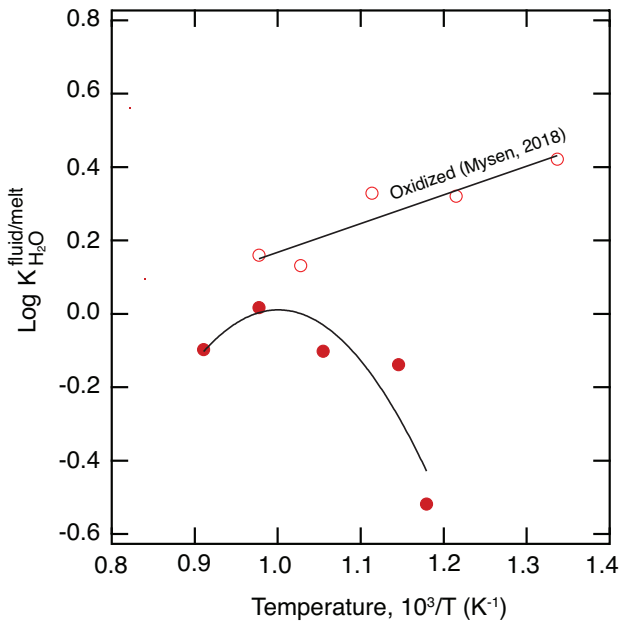


Figure 10

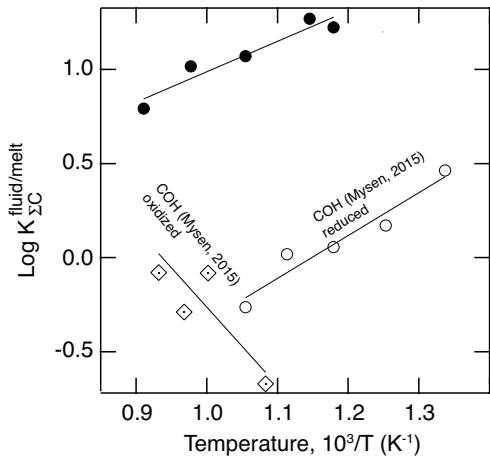


Figure 11

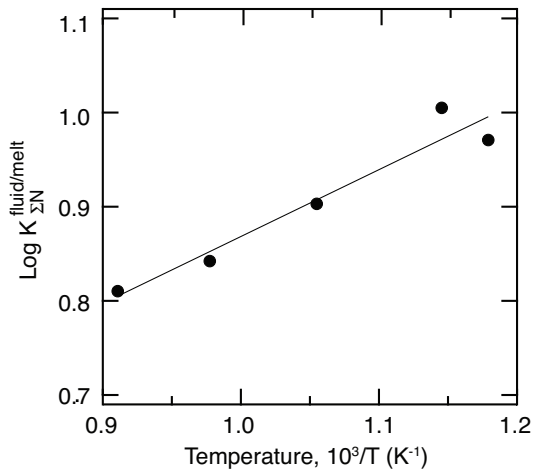


Figure 12

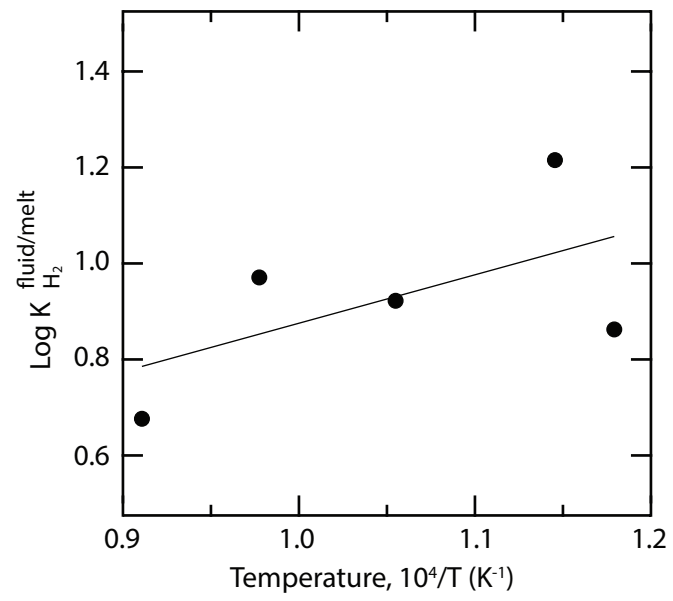


Figure 13